COMMUNICATION

Check for updates

Electrophoretic assisted fabrication of additive-free WS₂ nanosheet anodes for high energy density lithium-ion batteries†

Xuan-Manh Pham, [ID] ‡ Niraj Nitish Patil, [ID] ‡ Syed Abdul Ahad, Nilotpal Kapuria, [ID] Kwadwo Asare Owusu, Hugh Geaney, Shalini Singh [ID] and Kevin M. Ryan*

2D WS₂ nanosheets (NSs) are gaining popularity in the domain of Li-ion batteries (LIBs) due to their unique structures, which can enable reversible insertion and extraction of alkali metal ions. While synthesis methods have mostly relied on the exfoliation of bulk materials or direct growth on substrates, here we report an alternative approach involving colloidal hot-injection synthesis of 2D WS₂ in 2H and 1T′ crystal phases followed by their electrophoretic deposition (EPD) on the current collector. The produced 2D WS₂ NSs' films do not require any additional additives during deposition, which boosts the energy density of the additive-free LIBs produced. The 1T′ and 2H NSs exhibit long-term stable cyclic performance at C/5 for 600 cycles. At a high cycling rate (1C), the 2H NSs outperform the 1T′ NSs, delivering a 1st cycle reversible capacity of 513 mA h g⁻¹ with capacity retention of 73% after 100 cycles (compared to 205 mA h g⁻¹, and 84 mA h g⁻¹ respectively for NS-1T′). Post-cycling investigation confirms that there is no leaching or cracking of the active material on the surface of anodes after 100 cycles at C/5, which enables mechanical stability, and impressive battery performance of the WS₂ NS electrodes.

Introduction

The need for rechargeable batteries with high specific capacities, high power densities, and extended cycle lives is rising substantially each year due to the increased proliferation of electronic devices and electric vehicles.[1–5] The current state-of-the-art materials with limited specific capacity used in Li-ion batteries (LIBs) hinder the development of this technology (*e.g.* cathode (lithium cobalt oxide (LCO), 135 mA h g⁻¹)[6] and anode (graphite, 372 mA h g⁻¹)[7]). New anode materials for high-performance LIBs have been extensively researched, with examples including tran-

sition metal oxides,[8,9] metal–carbon composite materials,[10,11] and transition metal dichalcogenides (TMDs; general formula: MX₂, where M = (W, Mo, Zn, or Fe) and X = (S or Se)).[12–16] In general, TMDs exhibit structural similarity to graphite, with the ability to arrange into binary structures wherein the stacked atomic layers (X–M–X) are held together by van der Waals forces acting across the interlayer gaps.[12,17] Consequently, it is feasible to exfoliate bulk TMDs into single- or few-layered nanostructures, which facilitates Li⁺ intercalation reactions. According to the atomic stacking configurations, MX₂ materials primarily crystallize in two distinct phases: the trigonal prismatic (2H) phase and the octahedral (1T or 1T′) phase. In 2H phase, S atoms coordinate in a prismatic fashion around one W atom, giving semiconducting characteristics, whereas for 1T or 1T′ phase the six S atoms form octahedral co-ordination around one W atom, giving metallic character.[12,18] Belonging to the family of TMDs, WS₂ has a layered structure with a larger interlayer spacing (>6 Å) than graphite (3.55 Å), efficiently promoting Li ion diffusion, along with the high electron mobility and chemical stability.[19,20] Additionally, they also offer advantages such as low cost and high theoretical capacities (433 mA h g⁻¹), which makes them a good anode material for LIBs.[21,22] For instance, Yin *et al.*[17] reported a remarkable Li storage performance for WS₂ sheets grown on TiNb₂O₇ nanofibers, with a specific capacity of 627 mA h g⁻¹ after 200 cycles cycled at 1 A g⁻¹ and a specific capacity of 344 mA h g⁻¹ after 300 cycles cycled at 5 A g⁻¹ (∼12 C). Additionally, Liu *et al.*[23] prepared binder-free WS₂/reduced-graphene oxide (rGO) paper for LIBs, exhibiting a reversible capacity of 697.7 mA h g⁻¹ after 100 cycles. However, WS₂ based LIB electrodes have been mostly prepared *via* a slurry approach using binders and carbon additives to achieve good mechanical integrity and electrical conductivity. These electrochemically inactive binders and carbon additives typically constitute about 10–40 wt% of the electrode,[24,25] significantly impacting the energy density.

Electrophoretic deposition (EPD) is a versatile technique for fabricating electrodes without the use of any additives. In this technique, the current collector is dipped in a solution of charged nanocrystal (NC) materials which travel to its surface in

Department of Chemical Sciences and Bernal Institute, University of Limerick, Ireland. E-mail: Kevin.M.Ryan@ul.ie

‡These authors contributed equally to this study.

the presence of an applied electric field.[26] The EPD technique possesses several advantages over slurry processing, including improved layer conductivity,[5,27] the ability to uniformly deposit nanomaterials onto 3D surfaces[5,28] and the suitability for large-area processes.[5,29] For example, this approach has been used to create a wurtzite Cu_2ZnSnS_4 (CZTS) nanorods-based anode with a high specific capacity (1363 mA h g^{-1} after 100 cycles in a half cell and 604 mA h g^{-1} after 474 cycles in the full cell at 200 mA g^{-1}).[1] However, EPD has sparingly been used for the formation of anodes composed of 2D NS active materials, despite its use in electrocatalytic applications.[5,30]

Herein, EPD was used to prepare high performance WS_2 NSs Li-ion battery electrodes. The WS_2 NSs (1T′ and 2H phases) were synthesized using organic-phase colloidal methods, prior to EPD formation of binderless and carbon-free electrodes. At low current rates, the WS_2 electrodes (NS-1T′ and NS-2H) display stable cyclability. NS-2H outperformed the NS-1T′, retaining a capacity of 377 mA h g^{-1} after 100 cycles (capacity retention of 73%), compared to 84 mA h g^{-1} (capacity retention of 41%) respectively for NS-1T′ at 1C. Post-cycling characterization was used to elucidate the stable cycling performance of WS_2 electrodes prepared by EPD. There were no signs of leaching or cracking on the electrodes observed throughout the long cycling period. As such, this study represents the next stage in the investigation of colloidally synthesized TMD NCs for energy storage application.

Results and discussion

We synthesized colloidal WS_2 (2H and 1T′ dominated phases) by hot injection approach from the experimental procedure published earlier by our group.[18] The synthesized samples were thoroughly investigated using different characterization techniques. Fig. 1a shows the hot-injection technique for formation of WS_2 nanosheets (NSs) in two different crystal phases, where the 2H dominated and 1T′ dominated materials are denoted as a NS-2H and a NS-1T′, respectively. As shown in Fig. 2a, the Raman spectrum of NS-2H sample shows two peaks at the E^1_{2g} (350 cm^{-1}) and A_{1g} (415 cm^{-1}) modes, which indicates the presence of the 2H phase. For the NS-1 T′ sample, the suppression of E^1_{2g} and A_{1g} peaks and the appearance of two peaks at 182 (J_2) and 260 cm^{-1} (A_g) were observed, confirming its 1T′ dominated nature.[18,31] The UV–vis absorption spectra (Fig. 2b) reveal a broad absorption spectrum with no visible peaks for the NS-1T′ sample, while characteristic peaks were noted at ~437 nm, 520 nm and 615 nm for the 2H phase (NS-2H sample).[31,32]

XPS spectra further confirmed the metallic 1T′ and 2H phases based on the core level peaks of W $4f_{7/2}$, W $4f_{5/2}$, S $2p_{3/2}$ and S $2p_{1/2}$ in the XPS spectra (as shown in Fig. 2c and d). The two strong signals at 32.2 eV and 34.4 eV correspond to W^{4+} $4f_{7/2}$ and W^{4+} $4f_{5/2}$ within the 1T′ phase, respectively (Fig. 2c). The additional peaks at 33.2 eV and 35.4 eV are attributed to W^{4+} $4f_{7/2}$ and W^{4+} $4f_{5/2}$ of the 2H phase. The two peaks of W^{6+} at 35.9 eV and 38.1 eV indicate the partial oxidation of the nanosheets for the NS-1T′ sample.[12,18,31] The S_{2p} XPS spectra (Fig. 2d) displays S^{2-} $2p_{3/2}$ and S^{2-} $2p_{1/2}$ signals, including two main 1T′ phase peaks at 161.8 and 163.0 eV and two minor peaks of the 2H phase at 163.1 and 164.3 eV, which is in good agreement with the S 2p peak locations reported for 1T′ WS_2.[33] The peaks corresponding to the 1T′ phase are dominant in the sample denoted NS-1T′,
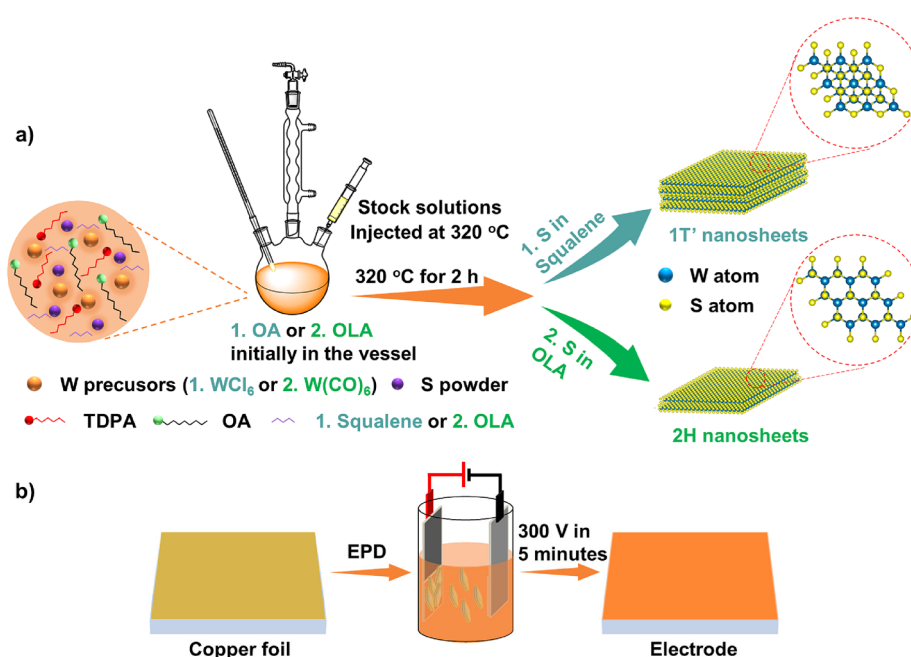
Fig. 1 (a) Schematic illustration of the synthesis process of WS_2 nanosheets (1T′ and 2H phases), (b) schematic illustration of electrode fabrication by using EPD.
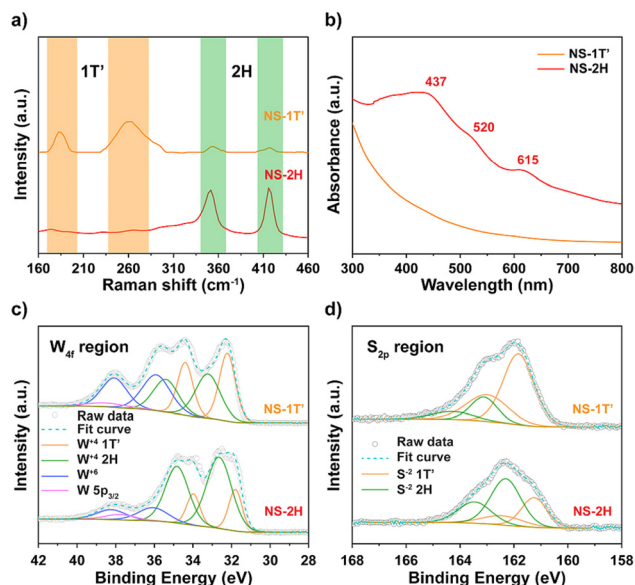
Fig. 2 (a) Raman spectra and (b) UV–vis spectra of NS-1T′ (orange) and NS-2H (red), (c) high-resolution W XPS spectra and (d) S XPS spectra of NS-1T′ and NS-2H.

while the peaks linked to the 2H phase predominate in the NS-2H sample. For the NS-2H material, the two main peaks occurred at 31.8 and 34.0 eV in the W 4f, corresponding to the respective levels of 2H WS$_2$ phase, while the two

additional peaks at 32.7 and 34.8 eV are the characteristic of 1T′ phase WS$_2$ and the minor peaks at 36.1 and 38.2 eV can be attributed to partially oxidized WS$_2$ (Fig. 2c).[18,31,33] Similarly, the two strong peaks of S 2p$_{3/2}$ and S 2p$_{1/2}$ from the 2H phase were positioned at 162.4 and 163.5 eV, respectively, and both additional peaks are identified at high energies of metallic 1T′ phase (Fig. 2d).[34] The XRD patterns of NS-1T′ and NS-2H samples are presented in Fig. S1a (ESI†). The 1T′ phase and 2H phase can be identified based on XRD peaks in the areas of 31–32° and 56–59°. The XRD peaks at ~32.5° and 57.1° are linked to the (100) and (008) planes of the 1T′ phase, while the peaks at ~33.0° and 58.3 correspond to the (101) and (110) planes of the 2H phase.

The TEM images (Fig. 3a and f) confirmed the successful synthesis of WS$_2$ NSs (NS-1T′ and NS-2H). The nanosheet morphology of WS$_2$ can be observed in TEM images from different areas (Fig. S2, ESI†). HR-TEM images (Fig. 3b and g) reveal stacked layers of nanosheets for both NS-1T′ and NS-2H samples, respectively. The clear (100) lattice fringes with a *d*-spacing of 2.73 Å characteristic for 1T′ phase was identified (Fig. S1b, ESI†). The NS-2H sample (Fig. S1c, ESI†) showcases an atomic honeycomb-like configuration with a *d*-spacing of 2.7 Å, matching the (101) planes, which are the distinguishing characteristics of the 2H phase. These findings are in agreement with the XRD results. The EDX maps of NS-1T′ (Fig. 3d and e) and NS-2H (Fig. 3i and j), along with the scanning-TEM (STEM) images of NS-1T′ (Fig. 3c) and NS-2H (Fig. 3h), respect-
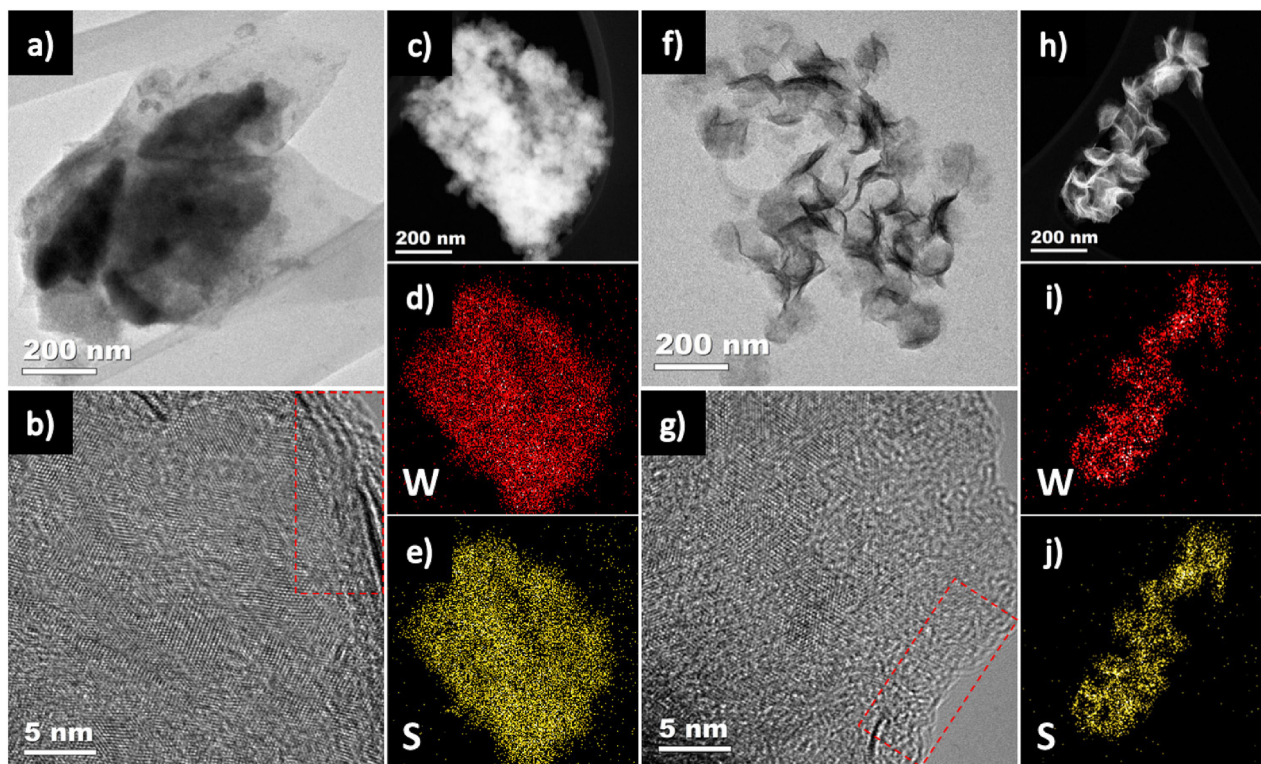
Fig. 3 (a) TEM image, (b) HR-TEM image, and (c) STEM of NS-1T′ with (d and e) corresponding elemental mapping for W and S. (f) TEM image, (g) HR-TEM image, and (h) STEM of NS-2H with (i and j) corresponding elemental mapping for W and S.
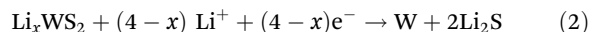
ively, indicate the uniform distribution of S and W throughout the materials.

The electrochemical characteristics of WS$_2$ NS as an anode material for LIBs were investigated *via* galvanostatic charge–discharge (GCD) cycling, cyclic voltammetry (CV) and electrochemical impedance spectroscopy (EIS). The WS$_2$ NS electrodes were prepared *via* EPD (Fig. 1b), wherein two Cu foils were immersed parallel in the solution bath. Under the electric field generated by a DC voltage of 300 V, the charged NSs moved and deposited onto the Cu foil to form a film of NSs. SEM images of the films show a uniform network of deposited NS-1T′ (Fig. S3a, ESI†) and NS-2H (Fig. S3b, ESI†). A dense and uniform film is extremely important for battery applications as it ensures a continuous electrical conducting network throughout the film. Fig. 4 demonstrates the impact of the crystal phase on the electrochemical performance of WS$_2$ through the galvanostatic discharge–charge cycling test of NS-2H and NS-1T′ at C/5 (~86 mA g^{-1}). The lithiation/delithiation of WS$_2$

in LIBs is governed by the following reversible intercalation and irreversible conversion reactions:

$$x\text{Li}^+ + \text{WS}_2 + x\text{e}^- \leftrightarrow \text{Li}_x\text{WS}_2 \qquad (1)$$

$$\text{Li}_x\text{WS}_2 + (4-x)\,\text{Li}^+ + (4-x)\text{e}^- \rightarrow \text{W} + 2\text{Li}_2\text{S} \qquad (2)$$

Two-stages of intercalation-conversion process are typically what control the lithiation of TMD materials (WS$_2$, MoS$_2$, and WSe$_2$).[12,17,35–37] During the lithiation, Li ions intercalate into WS$_2$, generating an intermediate Li$_x$WS$_2$ structure. Then, this structure is converted to form Li$_2$S along with metallic W.[37] The delithiation process then restores the original WS$_2$ structure from the Li$_x$WS$_2$ intermediate structure and forms elemental S as a coexisting phase (with WS$_2$).[17,37–40]

Fig. 4a and b shows the charge/discharge profiles of NS-1T′ and NS-2H, respectively. Firstly, Li intercalation into NS-1T′ (Fig. 4a) occurs at the discharge slope starting from ~1.7 V to 0.5 V, then conversion reaction takes place from 0.5 V to 0.01 V
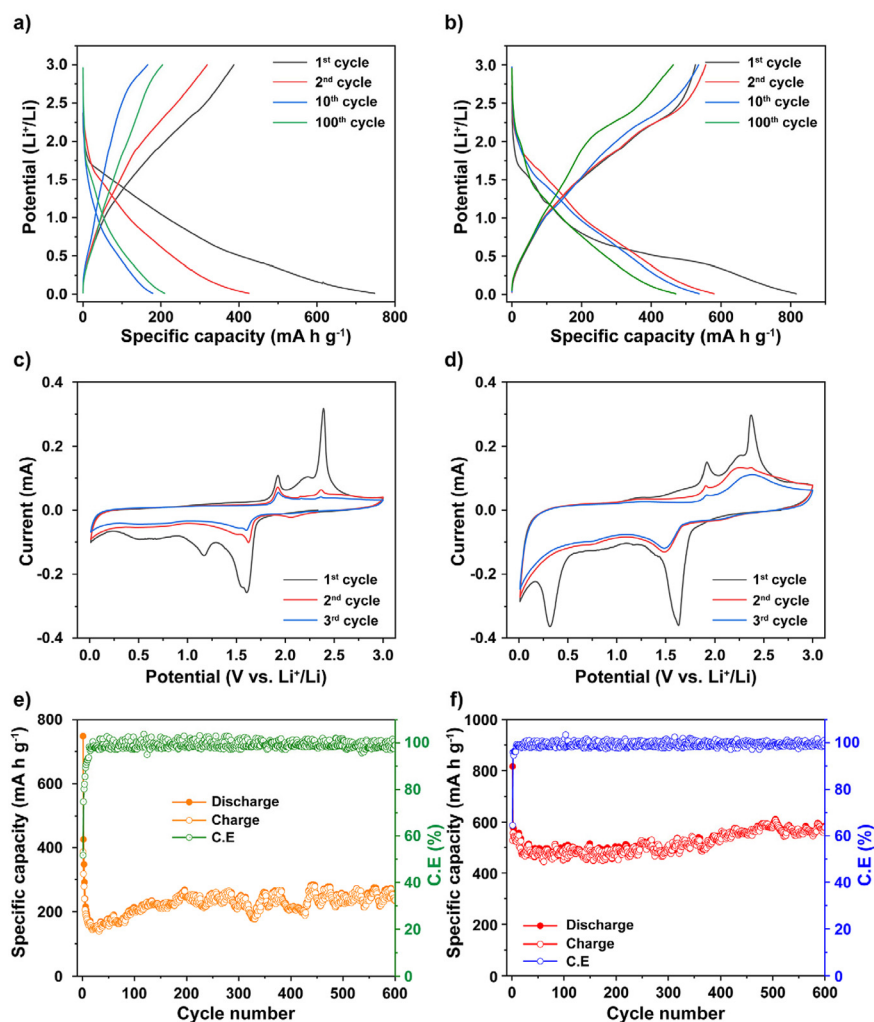
Fig. 4 1st, 2nd, 10th and 100th discharge/charge profiles of (a) NS-1T′ and (b) NS-2H electrodes at a rate of C/5, cyclic voltammograms of (c) NS-1T′ and (d) NS-2H electrodes recorded at a scan rate of 0.05 mV s^{-1}, cyclability of and coulombic efficiency of (e) NS-1T′ and (f) NS-2H at a rate of C/5.

in the first cycle. In the initial charge, the charge voltage increased gradually from 0.01 to 3.0 V, there are no distinctive plateaus observed. In the subsequent cycles, the insertion/extraction of Li$^+$ and conversion reactions could not be recognised distinctively, with gradual discharge and charge profiles. The absence of any distinct (de)lithiation features in the GCD profiles of NS-1T′ suggests the restriction of Li intercalation into NS-1T′, which may in turn result in the low specific capacity. In contrast, NS-2H exhibits a charge–discharge behaviour typical of WS$_2$ (Fig. 4b). The initial discharge curve revealed two Li insertion plateaus at 1.7 V and 1.0 V, along with a slope descending from 0.5 V to the cutoff voltage of 0.01 V.[41] The charge voltage increased progressively throughout the initial charge, linked to the delithiation of the Li$_x$WS$_2$, before experiencing a brief plateau around 2.3 V *versus* Li/Li$^+$, corresponding to the delithiation of the Li$_2$S. The discharge plateau from the subsequent cycles shows a new peak situated at around 2.0 V, which can not be distinctly seen in the GCD profiles of NS-1T′. This plateau relates well with the reaction of S with Li$^+$ to form Li$_2$S.[38,40,42–46] The existence of elemental S domains was explained by the delithiation of Li$_2$S which also maintains W elements as an electrochemically inert buffer because W could not react with S to revert to WS$_2$.[40,42–45] Having both of these two species (*i.e.* W and Li$_2$S) at the discharged state of the electrode offers two advantages. Firstly, the metallic W buffer has a favourable impact on the electrode's overall electronic conductivity. Secondly, elemental S, which is produced after the initial WS$_2$ lithiation–delithiation process, participates in subsequent charge and discharge loops that contribute to a larger specific capacity of the electrodes as the theoretical capacity of S is 1675 mA h g^{-1}.[40,42–45] These reasons explain why NS-2H exhibits a superior capacity and performance compared to NS-1T′. The successive cycles' discharge and charge curves of both NS-1T′ and NS-2H almost completely overlap, demonstrating the remarkable stability of the active material's structure.

Consistent with the GCD studies, the cathodic scan of NS-1T′ (Fig. 4c) shows the series of three cathodic processes from 1.7 V to 0.01 V in the first cycle, attributed to (1) the formation of solid electrolyte interface (SEI) layer on WS$_2$ surface;[23,38] (2) the Li$^+$ intercalation into WS$_2$ layers; and (3) the conversion reaction of Li$_x$WS$_2$ to form elemental W and Li$_2$S.[40,42–45,47–49] During the first anodic scan, peaks at 1.8 V and 2.35 V *versus* Li$^+$/Li, are consistent mainly with the delithiation of residual Li$_x$WS$_2$ and Li$_2$S, respectively.[40,42–45,47–49] These behaviours are similar to NS-2H samples in the first cycle (Fig. 4d). In the second cathodic scan, a peak around 2.0 V was identified for both samples. However, this peak seemed to be minimised in the third cathodic scan of NS-1T′, while it remained in the NS-2H. This peak refers to the delithiation of Li$_2$S to form elemental S domains, a part of which did not react with W to restore the WS$_2$ structure. Therefore, elemental S could take part in the subsequent discharge process to increase the capacity of NS-2H, compared to NS-1T′. It is worth noting that the participation of S in the subsequent CD loops resembles the redox chemistry of S cathodes in Li–S batteries.

Hence, soluble high-order polysulfides (Li$_2$S$_n$, $3 \leq n \leq 8$) could be formed and the dissolutions of the soluble polysulfides might occur during cycling. However, in this situation, the W/WS$_2$ network[46,50,51] and SEI layer[52,53] established during the first lithiation can act together to reduce polysulfide diffusion effects and anode capacity fading. The subsequent cycles (the second and third cycles) of both electrodes exhibited unchanged positions of redox peaks, indicating that the WS$_2$-anodes have reached a reversible electrochemical behaviour after the first cycle.[38] The cyclic performance of NS-1T′ and NS-2H are shown in Fig. 4e and f. NS-1T′ delivers an initial specific capacity of ~748 (discharge) and 387 (charge) mA h g^{-1}, corresponding to a coulombic efficiency (CE) of ~51% (Fig. 4e). On the other hand, NS-2H exhibits a better initial specific capacity of ~816 (discharge) and 527 (charge) mA h g^{-1}, corresponding to a coulombic efficiency (CE) of ~64% (Fig. 4f). The low initial coulombic efficiencies of both electrodes were caused by the high consumption of Li$^+$ to form the SEI layer. However, the CEs rose swiftly, reaching >95% after 10 cycles and becoming stable thereafter. In the subsequent cycles, there were three distinct phases of cell performance that could be distinguished: (1) an initial rapid capacity decrease, (2) a recovery, and (3) a stabilization of capacity. Similar stability tendencies have previously been seen for other sulfide materials[1,54–56] with the recovery or increase in capacity, which is frequently linked to the "activation" of the material,[57] and is also associated with a reduction in electrode impedance. The specific capacity of NS-1T′ dropped to ~146 (discharge) and 144 (charge) mA h g^{-1} after 20 cycles (63% capacity drop), then increased and stabilized around ~239 (discharge) and 237 (charge) mA h g^{-1} after 600 cycles (~capacity retention of 64%). The low specific capacity of NS-1T′ (less than the theoretical capacity of WS$_2$, 433 mA h g^{-1}) is mainly because of the restriction of Li intercalation, explained in the GCD profiles of NS-1T′. Conversely, the initial drop in the capacity of NS-2H was less severe (12% capacity drop) after 20 cycles and the specific capacity stabilized and reached 580 (discharge) and 579 (charge) mA h g^{-1} after 600 cycles, which are higher than the initial specific capacity. The improved specific capacity of NS-2H (higher than the theoretical capacity of 433 mA h g^{-1}) was explained to be linked to the contribution of S element in the discharge/charge loops previously. Moreover, depending on the phase structure of WS$_2$ (or other TMDs) which facilitates the Li insertion, the achieved reversible capacity will be greater than the theoretical capacity. For instance, Julien *et al.*[58] discovered that only 0.6 mole of Li$^+$ per one mole of crystalline WS$_2$ was inserted to crystalline WS$_2$ powders, whereas Dominko *et al.*[59] reported that the quality of the MoS$_{2-x}$I$_y$ nanotubes affected the amount of Li$^+$ (1.7–3.0 mol) that could be inserted to one mole of MoS$_{2-x}$I$_y$. Similarly, Wang *et al.*[22] showed that WS$_2$ nanotube electrodes could give a reversible capacity of above 500 mA h g^{-1} (~4.7 mol Li per mole of WS$_2$) and Feng *et al.*[41] indicated that 7.4 mol Li per mole of WS$_2$ (~790 mA h g^{-1}) lithiated into WS$_2$ flakes. We compared the electrochemical performance of the as-prepared WS$_2$ NS anode with those of previously reported WS$_2$, in Table S1.†

The rate capability of WS_2 nanosheets was investigated at various rates (from C/10 to 10C for 5 cycles at each C-rate). As shown in Fig. 5a, the NS-2H exhibited a capacity of 652 mA h g^{-1}, 620 mA h g^{-1}, 574 mA h g^{-1}, 511 mA h g^{-1}, 411 mA h g^{-1}, 272 mA h g^{-1}, and 100 mA h g^{-1} at C/10, C/5, C/2, C, 2C, 5C, and 10C respectively. The NS-1T′, however, could not achieve high capacities at low current densities of C/10 (416 mA h g^{-1}), C/5 (376 mA h g^{-1}), C/2 (287 mA h g^{-1}) and did not cycle at high current densities of 5C, and 10C. Once the current density was returned to C/10, the specific capacity of NS-1T′ returned to 390 mA h g^{-1} (93% of the original capacity), whereas NS-2H achieved a capacity of 637 mA h g^{-1} (97.3% of the original capacity). Both NS-1T′ and NS-2H exhibited good stability over a wide range of C-rates because the lithiation of WS_2 nanosheets causes low volumetric expansion ($\sim$100%)[38,60–62] compared to alloying anodes (Si, Ge, and Sn). To illustrate the superior performance of NS-2H compared to NS-1T′, the NS-1T′ and NS-2H electrodes underwent cycling tests at a high rate of 1C ($\sim$433 mA g^{-1}). The electrodes were first cycled at a low rate of C/10 for five cycles prior to cycling at a comparatively high rate of 1C. As seen in Fig. 5b, NS-2H delivered a reversible capacity of 513 mA h g^{-1} at 1C in the first cycle (in total the sixth cycle) and maintained a high capacity of 377 mA h g^{-1} after 100 cycles (capacity retention of 73%, equivalent to a capacity loss of 0.28% per cycle). Conversely, NS-1T′ exhibited a low reversible capacity of 205 mA h g^{-1} in the first cycle at 1C and retained a capacity of 84 mA h g^{-1} after 100 cycles (capacity retention of 41%, corresponding to a capacity loss of 0.62% per cycle). In addition, the NS-2H electrode delivered better reversibility compared to the NS-1T′ electrode. The

coulombic efficiency of the NS-2H electrode grew significantly to a high value of 98% after five cycles and stayed steady at 99% after that, whereas the NS-1T′ electrode only rose to 94% after 5 cycles and 98% after 10 cycles (Fig. 5b). The lower rate capability of the 1T′ phase WS_2 compared to the 2H phase, despite its metallic nature, could be a result of both structural distortions and ion transport limitations. Although the 1T′ phase exhibits higher electrical conductivity, the octahedral coordination around the tungsten atoms introduces significant structural deformations, such as those caused by the Jahn–Teller effect. These deformations disrupt the ion transport pathways, impairing efficient diffusion and reducing rate capability. Conversely, the 2H phase, with its prismatic coordination, has a more stable and less distorted structure, allowing for smoother ion transport. Despite the superior conductivity of the 1T′ phase, its structural distortions and ion transport inefficiencies undermine its performance at higher rates. Additionally, the colloidal synthesis method used in our work also plays a role. The presence of ligands could further affect the 1T′ phase, potentially altering conductivity pathways or introducing resistive interfaces, contributing to the overall reduction in performance. To understand why NS-2H performs better than NS-1T′, electrochemical impedance spectroscopy (EIS) was carried out. Fig. 5c and d shows the Nyquist plots of the NS-1T′ and NS-2H fitted with an equivalent circuit model (Fig. S4, ESI†), respectively. The fitted EIS data are listed in Table S2 (ESI†). The R_{SEI} of both NS-1T′ and NS-2H remained similar over the number of cycles, which signifies stable SEI formation during cycling. Besides, both R_s and R_{ct} of NS-1T′ and NS-2H significantly decreased during the cycling. NS-1T′ had a higher R_s of 100
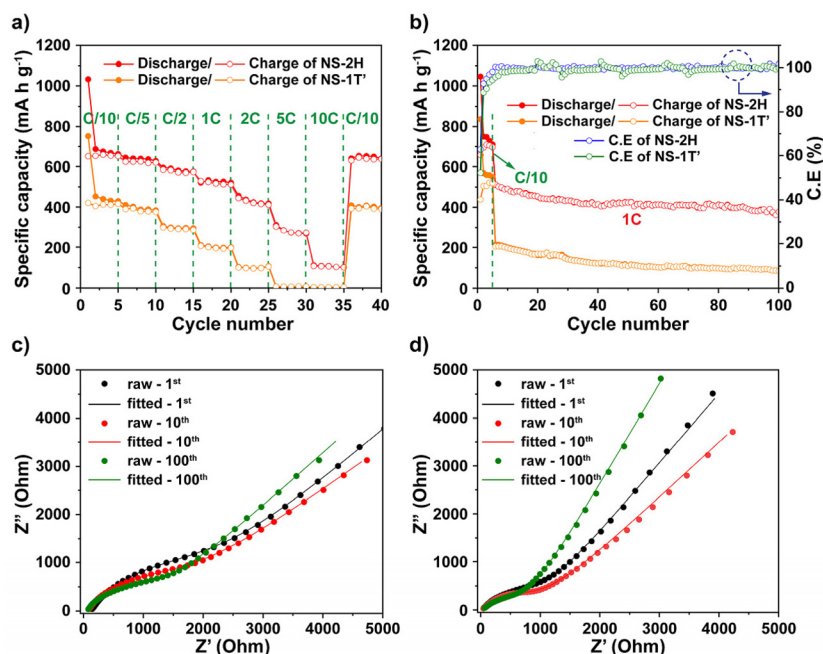
Fig. 5 (a) Rate capability testing of NS-1T′ and NS-2H electrodes at different current densities varying from C/10 to 10C, (b) cyclability and coulombic efficiency of the NS-1T′ and NS-2H electrodes at a rate of 1C, the first 5 cycles were performed at a low current rate of C/10, Nyquist plot of (c) NS-1T′ and (d) NS-2H.

Ohm and R_{ct} of 2317 Ohm after the first delithiation, then reduced to 61 Ohm (R_s) and 1490 Ohm (R_{ct}) after 100 cycles, while R_s and R_{ct} of NS-2H was 26 Ohm and 1110 Ohm (first delithiation), and 18 Ohm and 701 Ohm after 100 cycles, respectively. This indicates good active material interaction with the current collector, which is advantageous for electron transport during the electrochemical Li insertion/extraction reactions. However, the Nyquist plots of NS-1T′ displayed a significantly larger semicircle than the NS-2H, meaning a larger electrochemical reaction resistance compared to NS-2H. In particular, the charge transfer resistance of NS-1T′ is almost double that of NS-2H. This is deemed to be the main reason why NS-1T′ could not perform well at a high rate as a higher impedance causes more polarization. The effect of high impedance on the cell performance can be seen in detail in Fig. S5 (ESI†). At a high current rate of 1C, the discharge–charge curves of NS-2H (Fig. S5b, ESI†) still exhibited similar plateau potentials

as the low current rate of C/10, whereas only steep slopes of discharge–charge profiles were observed in NS-1T′ (Fig. S5a, ESI†).

To explain why the NS-2H WS_2 electrodes exhibited superior cycling stability for extended cycles, post-mortem of both types of WS_2 electrode was examined. Optical pictures of the untested WS_2 electrodes and the electrodes in their fully charged state following 100 cycles showed no clear difference (Fig. S6, ESI†). The surface of the WS_2 electrodes (both NS-1T′ and NS-2H) did not exfoliate even after 100 cycles of complete discharge and charge, demonstrating the stable attachment of the active material to the current collector, showing the excellent mechanical stability of the electrode prepared by EPD without additives (binder and conductive materials). This was also demonstrated using SEM analysis, which showed good material adhesion with the current collector, alongside a crack-free surface for the electrodes (NS-2H, Fig. 6a, b and NS-1T′, Fig. S7a, b, ESI†) after a long cycling period. The
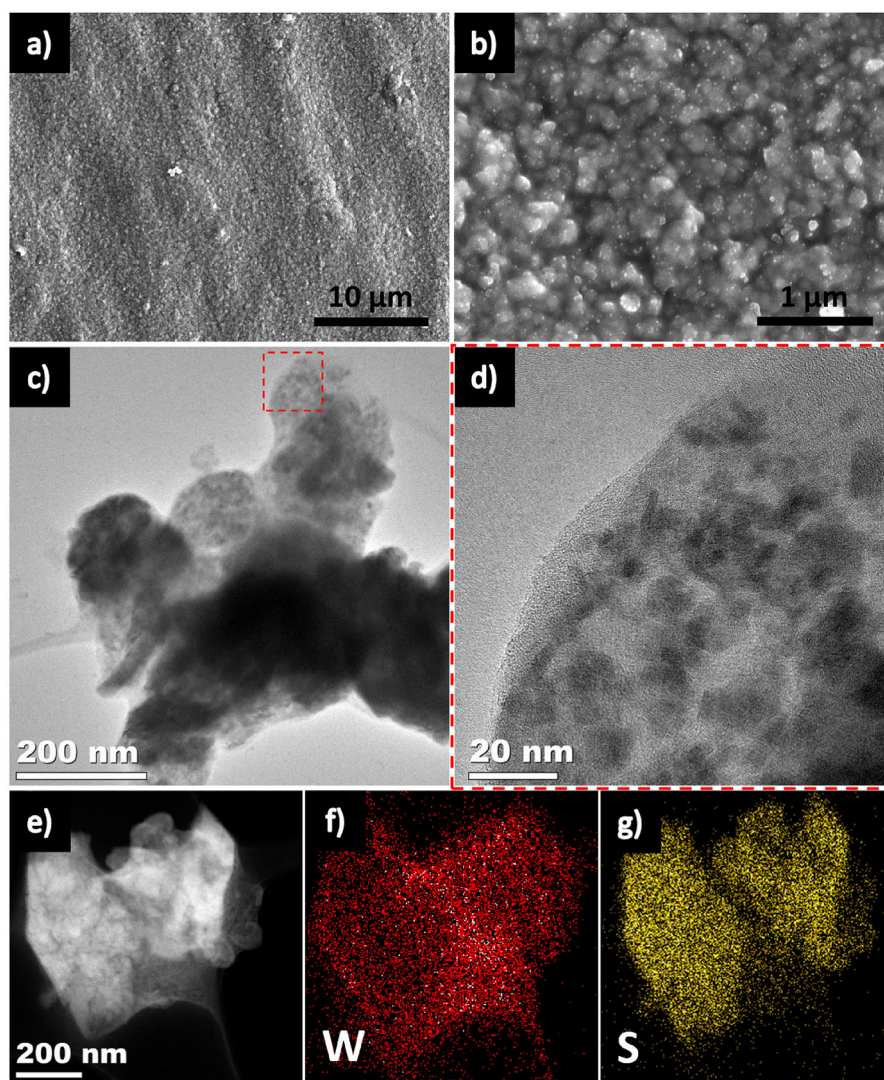
Fig. 6 Post-mortem after 100 cycles of WS_2 2H: (a and b) SEM images, (c and d) TEM images, (e) STEM image and (f and g) elemental mapping of W and S of the NS-2H sample.

NS-2H (Fig. 6c and d) and NS-1T′ (Fig. S7c and d, ESI†) appeared to undergo a change, losing the nanosheet morphology compared to pristine nanosheet structure. Furthermore, the mapping profile of NS-2H (Fig. 6f and g) and NS-1T′ (Fig. S7f and g, ESI†), along with the scanning-TEM (STEM) pictures (Fig. 6e and Fig. S7e, ESI†), respectively, confirmed that S and W elemental distribution was preserved in the NS even after 100 cycles.

Further structural analysis using HRTEM and SAED demonstrated that the NS-2H phase retains a higher degree of crystallinity compared to the NS-1T′ phase. The 2H phase preserves its layered structure more effectively, attributed to its greater thermodynamic stability (Fig. S8, ESI†). This stability enhances its resistance to degradation, resulting in better electrochemical performance. Conversely, the NS-1T′ phase demonstrates significant structural disorder, with a substantial portion of the 1T′ WS_2 converting into an amorphous structure after 100 cycles (Fig. S10, ESI†). Although some crystalline regions persist, they exhibit considerable fragmentation (Fig. S11, ESI†). This structural instability and fragmentation likely account for the inferior electrochemical performance of the 1T′ phase compared to the 2H phase. Additionally, high-resolution transmission electron microscopy (HRTEM) images of both the NS-2H and NS-1T′ phases post-cycling reveal the presence of tungsten (W) nanoparticles in conjunction with the WS_2 layers. These W nanoparticles, observable in both HRTEM images and selected area electron diffraction (SAED) patterns, are likely the result of an irreversible conversion reaction that occurred during the initial cycles (Fig. S9 & S11, ESI†). In general, both WS_2 phases showed good cycling ability due to minimal active material agglomeration and pulverization as evident by microscopy analysis.

Conclusions

In this work, the synthesis of WS_2 2H nanosheets and 1T′ nanosheets *via* a colloidal hot-injection method and the EPD based fabrication of binder-less and carbon-less battery electrodes were accomplished. 2H nanosheets achieved a capacity of 579 mA h g^{-1} after 600 cycles, while 1T′ nanosheets delivered a charge specific capacity of 237 mA h g^{-1} after 600 cycles. The enhanced performance of the 2H nanosheets was explained by the high electrical conductivity, low charge-transfer resistance and strong mechanical integrity of the EPD produced electrodes. Rate capability testing again demonstrated superior performance for the NS-2H, which had a specific capacity of 272 mA h g^{-1}, and 100 mA h g^{-1} at 5C, and 10C respectively, while NS-1T′ did not cycle. The good electrical connection, mechanical stability, and battery performance of the WS_2 NS electrodes fabricated by EPD were further elucidated by a thorough post-mortem study of these anode samples that included optical imaging, SEM, and TEM. In combination, this report represents the next stage in utilizing colloidal TMD NCs for battery electrodes using a binder-free, carbon-free and robust electrode manufacturing process.

Author contributions

All authors have given approval to the final version of the manuscript.

Conflicts of interest

There are no conflicts to declare.

Acknowledgements

References

1 G. Bree, H. Geaney, K. Stokes and K. M. Ryan, *J. Phys. Chem. C*, 2018, **122**, 20090–20098.

2 S. Abdul Ahad, S. Bhattacharya, S. Kilian, M. Ottaviani, K. M. Ryan, T. Kennedy, D. Thompson and H. Geaney, *Small*, 2023, **19**, 2205142.

3 V. Etacheri, R. Marom, R. Elazari, G. Salitra and D. Aurbach, *Energy Environ. Sci.*, 2011, **4**, 3243–3262.

4 P. V. Chombo and Y. Laonual, *J. Power Sources*, 2020, **478**, 228649.

5 A. Hajizadeh, T. Shahalizade, R. Riahifar, M. S. Yaghmaee, B. Raissi, S. Gholam, A. Aghaei, S. Rahimisheikh and A. S. Ghazvini, *J. Power Sources*, 2022, **535**, 231448.

6 F. Schipper, E. M. Erickson, C. Erk, J.-Y. Shin, F. F. Chesneau and D. Aurbach, *J. Electrochem. Soc.*, 2017, **164**, A6220.

7 V. Aravindan, Y.-S. Lee and S. Madhavi, *Adv. Energy Mater.*, 2015, **5**, 1402225.

8 M. E. Im, D. Pham-Cong, J. Y. Kim, H. S. Choi, J. H. Kim, J. P. Kim, J. Kim, S. Y. Jeong and C. R. Cho, *J. Power Sources*, 2015, **284**, 392–399.

9 L. Yin, Y. J. Gao, I. Jeon, H. Yang, J.-P. Kim, S. Y. Jeong and C. R. Cho, *Chem. Eng. J.*, 2019, **356**, 60–68.

10 Y. Liu, B. Yuan, C. Sun, Y. Lu, X. Lin, M. Chen, Y. Xie, S. Zhang and C. Lai, *Adv. Funct. Mater.*, 2022, **32**, 2202771.

11 R. Tian, H. Duan, Y. Guo, H. Li and H. Liu, *Small*, 2018, **14**, 1802226.

12 P. Zhou, G. Collins, Z. Hens, K. M. Ryan, H. Geaney and S. Singh, *Nanoscale*, 2020, **12**, 22307–22316.

13 L. Peng, Y. Zhu, D. Chen, R. S. Ruoff and G. Yu, *Adv. Energy Mater.*, 2016, **6**, 1600025.

14 D. H. Youn, C. Jo, J. Y. Kim, J. Lee and J. S. Lee, *J. Power Sources*, 2015, **295**, 228–234.

15 F. Qi, J. He, Y. Chen, B. Zheng, Q. Li, X. Wang, B. Yu, J. Lin, J. Zhou, P. Li, W. Zhang and Y. Li, *Chem. Eng. J.*, 2017, **315**, 10–17.

16 J. He, P. Li, W. Lv, K. Wen, Y. Chen, W. Zhang, Y. Li, W. Qin and W. He, *Electrochim. Acta*, 2016, **215**, 12–18.

17 L. Yin, D. Pham-Cong, I. Jeon, J.-P. Kim, J. Cho, S.-Y. Jeong, H. Woo Lee and C.-R. Cho, *Chem. Eng. J.*, 2020, **382**, 122800.

18 N. Kapuria, N. N. Patil, A. Sankaran, F. Laffir, H. Geaney, E. Magner, M. Scanlon, K. M. Ryan and S. Singh, *J. Mater. Chem. A*, 2023, **11**, 11341–11353.

19 L. Liu, S. B. Kumar, Y. Ouyang and J. Guo, *IEEE Trans. Electron Devices*, 2011, **58**, 3042–3047.

20 H. Shi, H. Pan, Y.-W. Zhang and B. I. Yakobson, *Phys. Rev. B: Condens. Matter Mater. Phys.*, 2013, **87**, 155304.

21 W. Yang, J. Wang, C. Si, Z. Peng, J. Frenzel, G. Eggeler and Z. Zhang, *J. Mater. Chem. A*, 2015, **3**, 17811–17819.

22 G. X. Wang, S. Bewlay, J. Yao, H. K. Liu and S. X. Dou, *Electrochem. Solid-State Lett.*, 2004, **7**, A321.

23 Y. Liu, W. Wang, Y. Wang and X. Peng, *Nano Energy*, 2014, **7**, 25–32.

24 D.-H. Ha, M. A. Islam and R. D. Robinson, *Nano Lett.*, 2012, **12**, 5122–5130.

25 D. Wang, Y. Yu, H. He, J. Wang, W. Zhou and H. D. Abruña, *ACS Nano*, 2015, **9**, 1775–1781.

26 J. H. Dickerson, *Electrophoretic deposition of nanomaterials*, 2012, pp. 131–155.

27 O. O. Otelaja, D.-H. Ha, T. Ly, H. Zhang and R. D. Robinson, *ACS Appl. Mater. Interfaces*, 2014, **6**, 18911–18920.

28 L. Besra and M. Liu, *Prog. Mater. Sci.*, 2007, **52**, 1–61.

29 S. Ahmed and K. M. Ryan, *Chem. Commun.*, 2009, 6421–6423, DOI: 10.1039/B914478A.

30 R. Tanakit, W. Luc and J. B. Talbot, *ECS Trans.*, 2014, **58**, 1.

31 Z. Liu, N. Li, C. Su, H. Zhao, L. Xu, Z. Yin, J. Li and Y. Du, *Nano Energy*, 2018, **50**, 176–181.

32 B. Mahler, V. Hoepfner, K. Liao and G. A. Ozin, *J. Am. Chem. Soc.*, 2014, **136**, 14121–14127.

33 H.-U. Kim, V. Kanade, M. Kim, K. S. Kim, B.-S. An, H. Seok, H. Yoo, L. E. Chaney, S.-I. Kim, C.-W. Yang, G. Y. Yeom, D. Whang, J.-H. Lee and T. Kim, *Small*, 2020, **16**, 1905000.

34 T. A. J. Loh, D. H. C. Chua and A. T. S. Wee, *Sci. Rep.*, 2015, **5**, 18116.

35 Q. Li, Z. Yao, J. Wu, S. Mitra, S. Hao, T. S. Sahu, Y. Li, C. Wolverton and V. P. Dravid, *Nano Energy*, 2017, **38**, 342–349.

36 R. Bhandavat, L. David and G. Singh, *J. Phys. Chem. Lett.*, 2012, **3**, 1523–1530.

37 X. Zeng, Z. Ding, C. Ma, L. Wu, J. Liu, L. Chen, D. G. Ivey and W. Wei, *ACS Appl. Mater. Interfaces*, 2016, **8**, 18841–18848.

38 S. Bellani, F. Wang, G. Longoni, L. Najafi, R. Oropesa-Nuñez, A. E. Del Rio Castillo, M. Prato, X. Zhuang, V. Pellegrini, X. Feng and F. Bonaccorso, *Nano Lett.*, 2018, **18**, 7155–7164.

39 Y. Xu, K. Wang, Z. Yao, J. Kang, D. Lam, D. Yang, W. Ai, C. Wolverton, M. C. Hersam, Y. Huang, W. Huang, V. P. Dravid and J. Wu, *Small*, 2021, **17**, 2100637.

40 S. Zhou, J. Chen, L. Gan, Q. Zhang, Z. Zheng, H. Li and T. Zhai, *Sci. Bull.*, 2016, **61**, 227–235.

41 C. Feng, L. Huang, Z. Guo and H. Liu, *Electrochem. Commun.*, 2007, **9**, 119–122.

42 H. Li, K. Yu, H. Fu, B. Guo, X. Lei and Z. Zhu, *Phys. Chem. Chem. Phys.*, 2015, **17**, 29824–29833.

43 Y. Liu, W. Wang, H. Huang, L. Gu, Y. Wang and X. Peng, *Chem. Commun.*, 2014, **50**, 4485–4488.

44 Y. Du, X. Zhu, L. Si, Y. Li, X. Zhou and J. Bao, *J. Phys. Chem. C*, 2015, **119**, 15874–15881.

45 R. Chen, T. Zhao, W. Wu, F. Wu, L. Li, J. Qian, R. Xu, H. Wu, H. M. Albishri, A. S. Al-Bogami, D. A. El-Hady, J. Lu and K. Amine, *Nano Lett.*, 2014, **14**, 5899–5904.

46 G. Huang, H. Liu, S. Wang, X. Yang, B. Liu, H. Chen and M. Xu, *J. Mater. Chem. A*, 2015, **3**, 24128–24138.

47 Y. Jing, Z. Zhou, C. R. Cabrera and Z. Chen, *J. Mater. Chem. A*, 2014, **2**, 12104–12122.

48 D. Jariwala, V. K. Sangwan, L. J. Lauhon, T. J. Marks and M. C. Hersam, *ACS Nano*, 2014, **8**, 1102–1120.

49 M. Pumera, Z. Sofer and A. Ambrosi, *J. Mater. Chem. A*, 2014, **2**, 8981–8987.

50 X. Fang, X. Yu, S. Liao, Y. Shi, Y.-S. Hu, Z. Wang, G. D. Stucky and L. Chen, *Microporous Mesoporous Mater.*, 2012, **151**, 418–423.

51 X. Fang, C. Hua, X. Guo, Y. Hu, Z. Wang, X. Gao, F. Wu, J. Wang and L. Chen, *Electrochim. Acta*, 2012, **81**, 155–160.

52 S. Waluś, C. Barchasz, R. Bouchet, J.-C. Leprêtre, J.-F. Colin, J.-F. Martin, E. Elkaïm, C. Baehtz and F. Alloin, *Adv. Energy Mater.*, 2015, **5**, 1500165.

53 J. Xiao, J. Z. Hu, H. Chen, M. Vijayakumar, J. Zheng, H. Pan, E. D. Walter, M. Hu, X. Deng, J. Feng, B. Y. Liaw, M. Gu, Z. D. Deng, D. Lu, S. Xu, C. Wang and J. Liu, *Nano Lett.*, 2015, **15**, 3309–3316.

54 Q. Jiang, X. Chen, H. Gao, C. Feng and Z. Guo, *Electrochim. Acta*, 2016, **190**, 703–712.

55 Y. Ren, H. Wei, B. Yang, J. Wang and J. Ding, *Electrochim. Acta*, 2014, **145**, 193–200.

56 Y. Du, Z. Yin, J. Zhu, X. Huang, X.-J. Wu, Z. Zeng, Q. Yan and H. Zhang, *Nat. Commun.*, 2012, **3**, 1177.

57 S. Ni, T. Li and X. Yang, *Thin Solid Films*, 2012, **520**, 6705–6708.

58 C. M. Julien, *Mater. Sci. Eng., R*, 2003, **40**, 47–102.

59 R. Dominko, D. Arčon, A. Mrzel, A. Zorko, P. Cevc, P. Venturini, M. Gaberscek, M. Remskar and D. Mihailovic, *Adv. Mater.*, 2002, **14**, 1531–1534.

60 R. Fong, U. von Sacken and J. R. Dahn, *J. Electrochem. Soc.*, 1990, **137**, 2009.

61 H. Kim, G. Yoon, K. Lim and K. Kang, *Chem. Commun.*, 2016, **52**, 12618–12621.

62 J. Xu, Y. Dou, Z. Wei, J. Ma, Y. Deng, Y. Li, H. Liu and S. Dou, *Adv. Sci.*, 2017, **4**, 1700146.